11-2008

A Comparison Study of Three Polar Grids

Tsing-Chang Chen
Iowa State University, tmchen@iastate.edu

Jenq-Dar Tsay
Iowa State University, mjdtsay@gmail.com

William J. Gutowski Jr.
Iowa State University, gutowski@iastate.edu

A Comparison Study of Three Polar Grids

Abstract
The circumference of a latitude circle decreases toward the Poles, making it difficult to present meteorological field variables on equally spaced grids with respect to latitude and longitude because of data aggregation. To identify the best method for displaying data at the Poles, three different grids are compared that have all been designed to reduce data aggregation: the reduced latitude–longitude (RL) grid, the National Snow and Ice Data Center Equal-Area Special Sensor Microwave Imager (SSM/I) Earth (EA) grid, and the National Meteorological Center octagonal (OG) grid. The merits and disadvantages of these grids are compared in terms of depictions of the Arctic summer circulation with wind vectors, streamfunction, and velocity potential at 400 hPa where maximum westerlies are located. Using geostrophy, the 400-hPa streamfunction at high latitudes can be formed from geopotential height. In comparison with this geostrophic streamfunction, the streamfunction generated from vorticity on the OG grid shows a negligible error (~0.5%). The error becomes larger using vorticity on the EA (~15%) and RL (~30%) grids. During the northern summer, the Arctic circulation at 400 hPa is characterized by three troughs. The streamfunction and velocity potential of these three troughs are spatially in quadrature with divergent (convergent) centers located ahead of (behind) these troughs. These circulation features are best depicted by the streamfunction and velocity potential generated on the OG grid. It is demonstrated by these findings that the National Meteorological Center octagonal grid is the most ideal among the three grids used for the polar regions. However, this assessment is constrained by the hemispheric perspective of meteorological field variables, because these variables depicted on the octagonal grid at higher latitudes need to be merged with those on the equal-latitude-longitude grid at lower latitudes.

Keywords
Grid systems, Numerical analysis, Arctic, Streamfunction, Coordinate systems

Disciplines
Atmospheric Sciences | Climate

Comments
This article is from *J. Appl. Meteor. Climatol.*, **47**, 2993–3007. doi: http://dx.doi.org/10.1175/2008JAMC1746.1. Posted with permission.

NOTES AND CORRESPONDENCE

A Comparison Study of Three Polar Grids

TSING-CHANG CHEN, JENQ-DAR TSAY, AND WILLIAM J. GUTOWSKI JR.

Atmospheric Science Program, Department of Geological and Atmospheric Sciences, Iowa State University, Ames, Iowa

(Manuscript received 2 April 2007, in final form 18 March 2008)

ABSTRACT

The circumference of a latitude circle decreases toward the Poles, making it difficult to present meteorological field variables on equally spaced grids with respect to latitude and longitude because of data aggregation. To identify the best method for displaying data at the Poles, three different grids are compared that have all been designed to reduce data aggregation: the reduced latitude–longitude (RL) grid, the National Snow and Ice Data Center Equal-Area Special Sensor Microwave Imager (SSM/I) Earth (EA) grid, and the National Meteorological Center octagonal (OG) grid. The merits and disadvantages of these grids are compared in terms of depictions of the Arctic summer circulation with wind vectors, streamfunction, and velocity potential at 400 hPa where maximum westerlies are located. Using geostrophy, the 400-hPa streamfunction at high latitudes can be formed from geopotential height. In comparison with this geostrophic streamfunction, the streamfunction generated from vorticity on the OG grid shows a negligible error (~0.5%). The error becomes larger using vorticity on the EA (~15%) and RL (~30%) grids. During the northern summer, the Arctic circulation at 400 hPa is characterized by three troughs. The streamfunction and velocity potential of these three troughs are spatially in quadrature with divergent (convergent) centers located ahead of (behind) these troughs. These circulation features are best depicted by the streamfunction and velocity potential generated on the OG grid. It is demonstrated by these findings that the National Meteorological Center octagonal grid is the most ideal among the three grids used for the polar regions. However, this assessment is constrained by the hemispheric perspective of meteorological field variables, because these variables depicted on the octagonal grid at higher latitudes need to be merged with those on the equal-latitude-longitude grid at lower latitudes.

1. Introduction

The most commonly used reanalyses generated by global data assimilation systems of various operational centers [e.g., that of the National Centers for Environmental Prediction (Kanamitsu et al. 2002), the 40-yr European Centre for Medium-Range Weather Forecasts reanalysis (ERA-40; Uppala et at. 2005), and the Japanese 25-yr reanalysis project (Onogi et al. 2005)] are archived on the rectangular latitude–longitude (EL) grid with a 2.5° latitude × 2.5° longitude resolution. Because the radius of latitude circles is proportional to the cosine of the latitude, the circumference of latitude circles reduces toward the Poles. For example, from 47° to 70°N, the circumference of a latitude circle is almost halved. Meteorological data are often presented using an EL grid on a polar stereographic projection such as that shown in Fig. 1a. The analysis quality of some meteorological fields on this grid, such as wind vectors, may be degraded by the convergence of analysis points near the Poles. The closer analysis points allow smaller scales to be resolved, but there is no corresponding increase in constraining observations, so that the added smaller scales may not be weather/climate signals. The problem is exacerbated by gradients, which must be computed on a grid with spacing that becomes increasingly nonuniform as latitude increases. Analysis of meteorological data at high latitudes includes not only the first-order variables, but also their gradients and other variables derived from these gradients. Thus, the quality of the analysis at high latitudes may be degraded by the convergence of analysis points. Without special

Corresponding author address: Tsing-Chang (Mike) Chen, Atmospheric Science Program, Department of Geological and Atmospheric Sciences, Iowa State University, 3010 Agronomy Hall, Ames, IA 50011.
E-mail: tmchen@iastate.edu

DOI: 10.1175/2008JAMC1746.1

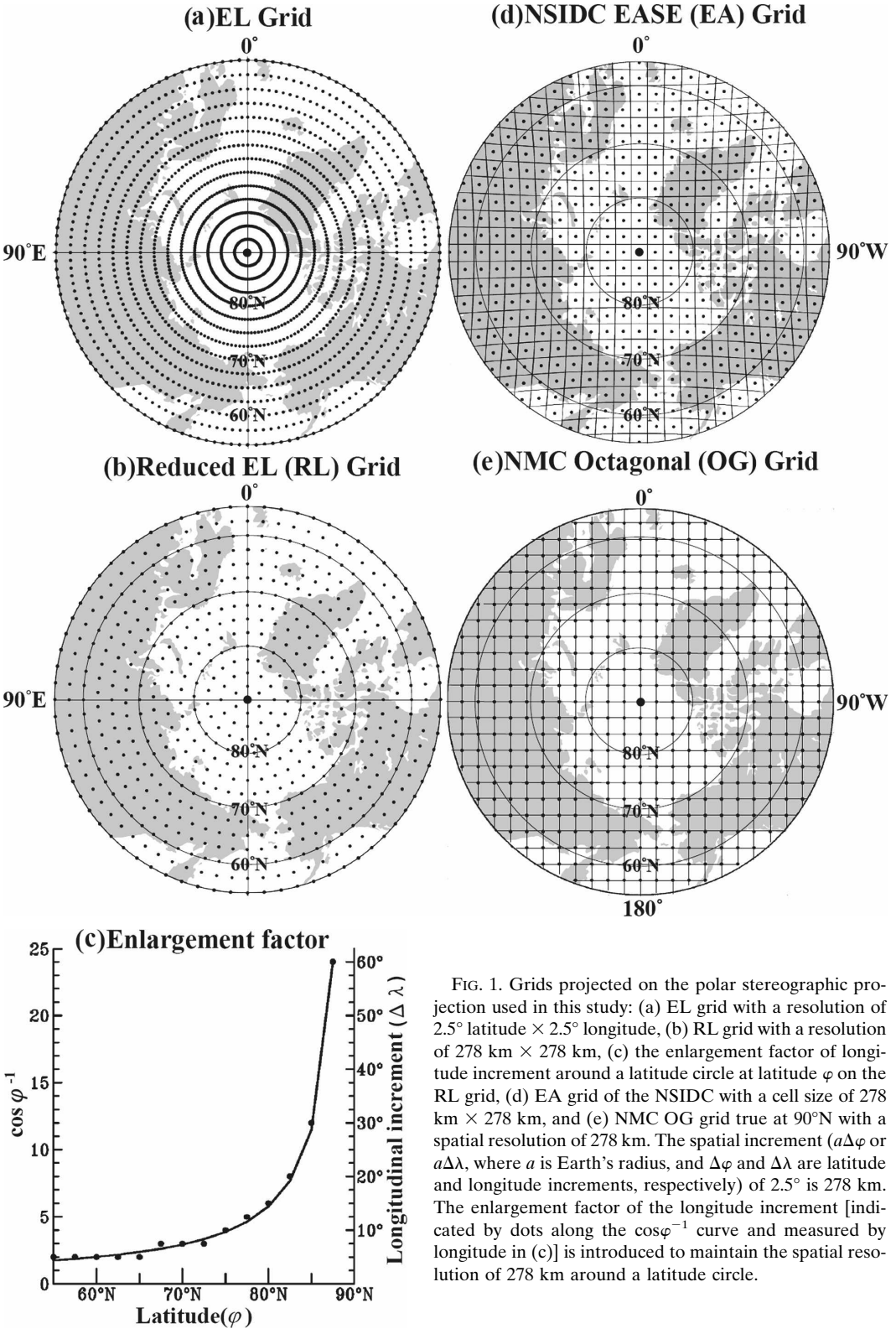

FIG. 1. Grids projected on the polar stereographic projection used in this study: (a) EL grid with a resolution of 2.5° latitude × 2.5° longitude, (b) RL grid with a resolution of 278 km × 278 km, (c) the enlargement factor of longitude increment around a latitude circle at latitude φ on the RL grid, (d) EA grid of the NSIDC with a cell size of 278 km × 278 km, and (e) NMC OG grid true at 90°N with a spatial resolution of 278 km. The spatial increment ($a\Delta\varphi$ or $a\Delta\lambda$, where a is Earth's radius, and $\Delta\varphi$ and $\Delta\lambda$ are latitude and longitude increments, respectively) of 2.5° is 278 km. The enlargement factor of the longitude increment [indicated by dots along the $\cos\varphi^{-1}$ curve and measured by longitude in (c)] is introduced to maintain the spatial resolution of 278 km around a latitude circle.

care, budget analyses of some variables (e.g., heat and vorticity) may not be accurate.

As revealed from the global energy budget, the polar regions are energy sinks caused primarily by the loss of energy through longwave radiation (e.g., Peixoto and Oort 1992). It has been reported by numerous studies [see the Intergovernmental Panel on Climate Change Fourth Assessment Report (Parry et al. 2007)] that Earth's climate system has warmed during the past century. Presenting the atmospheric response to this global warming in global energy sink regions properly using meteorological variables, their gradients, and variables derived from these gradients, may be challenging. The polar circulation undergoes an interannual variation associated with the Arctic Oscillation (Thompson and Wallace 2000; Thompson et al. 2000). Differences in the depiction of the polar circulation using different grids may hamper the identification and representation of interannual variation modes in the polar regions. A deformed depiction of the high-latitude circulation may lead to an erroneous perception and hinder the understanding of the structure and maintenance mechanism of this circulation. Our understanding of these potential differences may facilitate the identification of the anomalous polar circulation. To portray and analyze the polar circulation in the context of the hemispheric perspective in a more illustrative way, it is crucial to use an appropriate grid.

To portray properly the polar circulation and to perform budget analyses accurately, three different grid systems (their descriptions will be provided in section 2) developed on a plane surface have been introduced to maintain uniform spatial resolution and to reduce data aggregation near the Poles: 1) the reduced latitude–longitude (RL) grid (e.g., Kurihara 1965; Simmods 1978; Bormann and Thépaut 2004; DeWeaver and Bitz 2006), 2) the equal-area Special Sensor Microwave Imager (SSM/I) Earth (EASE, mostly referred to hereinafter as EA) grid developed by the National Snow and Ice Data Center (NSIDC; Armstrong and Brodzik 1995), and 3) the National Meteorological Center (NMC) octagonal (OG) grid (Shuman and Hovermale 1968; Jenne 1975). A systematic comparison of these grids has not been made, and this paper aims to address the advantages and differences between these grids to understand better their relative merits in depicting polar weather systems and circulation structures.

The atmospheric circulation and weather systems in the Arctic have been portrayed by most studies in past decades in terms of first-order variables (e.g., surface pressure, temperature, geopotential height, precipitation, snow, and ice), wind vectors, and moisture transport. The spatial structure and values of scalar variables are not changed by their depiction on different grids. In contrast, any analysis using components of wind vectors on the EA and OG grids requires a transformation of the components from those on the EL grid to those two grids. Otherwise, it is not possible to calculate gradients of wind components on the EA and OG grids without the aforementioned transformation, using the globally assimilated data archived on an EL grid. Furthermore, it has been shown that the atmospheric circulation can be depicted well by the streamfunction ψ and velocity potential χ (Krishnamurti 1971; Krishnamurti et al. 1973). The spatial χ–ψ relationship facilitates the search for the maintenance mechanisms of the atmospheric circulation (e.g., Chen 2005). Both ψ and χ are obtained by solving the Poisson equation with vorticity ζ and divergence D as input, respectively,

$$\nabla^2\psi = \zeta, \quad \text{where} \quad \zeta = \hat{k} \cdot \nabla \times \mathbf{V} \quad \text{and} \tag{1}$$

$$\nabla^2\chi = D, \quad \text{where} \quad D = \nabla \cdot \mathbf{V}. \tag{2}$$

However, calculations of ζ and D, and in turn ψ and χ, are greatly affected by the decrease in grid spacing toward the Poles on the EL grid. Because variables important in the depiction of the polar circulation (i.e., wind vectors, ψ, and χ) experience a degradation in analysis quality caused by the reduced grid spacing toward the Poles, a comparison study is made for the analysis of the summer Arctic circulation using wind vectors, ψ, and χ on the three aforementioned grids. For this study, brief descriptions of the three available grids are presented in section 2. Transformation from wind components along latitude and longitude of the EL grid to rows (ordinate) and columns (abscissa) of the EA (OG) grids and generation of the ψ and χ fields on the different grids are given in section 3. A comparison of the Arctic summer circulation depicted by wind vectors $\mathbf{V}$, ψ, and χ on the three grids is made in section 4, followed by concluding remarks in section 5.

2. Three grids

a. RL grid

The circumference of a latitude circle is $2\pi a \cos\varphi$, where $a = 6371$ km is Earth's radius and φ is the latitude. The factor of $\cos\varphi$ decreases when φ increases toward the Poles and vanishes at the Poles where $\varphi = \pm\pi/2$. In the EL grid on the polar stereographic projection (Fig. 1a), the spatial interval between two grid points along a latitude circle decreases toward the Poles. To reduce the aggregation of the EL grid points at high latitudes, and to maintain the uniformity of spatial resolution between grid points along latitude

circles, the most common approach in meteorology is to remove grid points by different factors (indicated by $\Delta\varphi$ along the ordinate in Fig. 1c) depending on latitude. An example of an RL grid is shown in Fig. 1b. Any meteorological field computed from another using this grid system should have less numerical error than that resulting from grid aggregation in the polar region at the expense of some details in the field. In other words, data aggregation is reduced, but degradation of analysis resolution is the result. Note that the spatial resolution along different latitude circles in the RL grid is not always uniform and depends on the enlargement factor of longitude increments along a latitude circle. Thus, any variable computed using spatial derivatives of other variables (e.g., vorticity and divergence) may be deformed relative to those generated using an appropriate grid. In turn, variables derived from these spatial derivatives (e.g., the streamfunction or velocity potential) are also deformed in the polar region.

b. NSIDC EASE grid

The SSM/I is operated by the Defense Meteorological Satellite Program and performs microwave observations of surface snow and ice cover. To produce an analysis of daily global snow cover, the NSIDC developed the EA grid (Fig. 1d) on which the SSM/I observations were projected with a resolution of 25 km (Armstrong and Brodzik 1995). Data from all satellite observations over grid cells for 24-h periods are averaged with a weighting factor of $1/d^2$ [inverse-distance-squared method, where d is distance; Galantowicz and England 1991]. The NSIDC EA grid consists of two azimuthal equal-area projections for the Northern and Southern Hemispheres, and a global cylindrical equal-area projection for low latitudes (Brodzik and Knowles 2002, chapter 5). At the time of writing, the software support and the mathematical details of this grid could be found on the NSIDC Internet site (http://www.nsidc.colorado.edu/data/ease/ease_grid. html and http://www.nsidc.org/data/ease/ease_grid.html).

The NSIDC EA grid was developed primarily to maintain the quality of analysis over regions with large nonuniformity in spatial resolution. Although the remotely sensed snow/ice cover data generated by NSIDC are first-order variables, this grid has been applied to prepare and to analyze diagnostically the high-resolution initial conditions for simulations by some regional climate models (e.g., Jürrens 1999). Important meteorological variables, like wind vectors, averaged over a 25 km $\times$ 25 km cell of the NSIDC EA grid are perhaps a good representation for any given location within the cell, because of its small size. Assimilated wind components are operationally archived on an EL grid with a resolution of 2.5° latitude $\times$ 2.5° longitude ($\sim$278 km $\times$ 278 km in the tropics). Wind components along rows and columns of the EA grid are needed to depict a synoptic-scale weather/climate system; components of the area-mean wind vectors calculated with those on the EL grid require a transformation.

c. NMC octagonal grid

The NMC OG grid is a regular mesh projected on the polar stereographic grid (true at 60°N) and is centered at the North Pole (Fig. 1 of Shuman and Hovermale 1968). For its operational six-layer primitive equation forecast model, the NMC prepared initial conditions on an OG grid that extended from the North Pole to about 20°N. On the other hand, initial conditions for its operational tropical forecast model were prepared on a Mercator grid covering the tropics from 48°S to 48°N (Bedient et al. 1967). To create a dataset covering the entire hemisphere, Burrows (1974) merged the NMC horizontal wind components (u, v) and temperature data analyzed on the OG and Mercator grids using a 16-point Bessel (B-16) interpolation scheme (Jenne 1975) over a latitudinal zone between 27° and 33°N. [At the time of writing, a FORTRAN program and details of this scheme could be found on the National Center for Atmospheric Research (NCAR) Internet site (http://dss.ucar.edu/libraries/gridinterps/polarinterps.html).] However, directions of wind vectors were not considered in this data merging process. Thus, the Burrows (1974) merging principle should be expanded to cover transformation of wind components from the EL grid to the OG grid when gradients of wind components used to compute vorticity and divergence are needed on the latter grid. Vorticity and divergence computed on the OG grid are then interpolated by the B-16 scheme back to the EL grid, so that a spherical harmonics analysis can be applied to solve the Poisson equation and to obtain the streamfunction and velocity potential. The OG grid was introduced when the NMC developed an operational primitive equation model four decades ago. Although this model is now obsolete, the NMC OG grid (Fig. 1e) is excellent for depicting the polar circulation and examining its dynamics (shown later in section 4).

3. Orientation of the grid

a. Wind vectors

Inspection of two arrays of grids on a polar-stereographic projection, as displayed in Figs. 1d and 1e, shows that the orientation of the OG grid is the same as the EA grid but the OG grid points deviate

from the centers of EA cells, except at the Pole. On the other hand, the orientation of both the EA and OG grids differs from the EL grid (Fig. 1a). The data archived on the EL grid can be easily displayed on the polar stereographic projection, regardless of the data aggregation problem toward the Poles. Note that scalar variables archived on the EL grid of a sphere can be projected directly onto the EL grid of the polar stereographic plane without a special procedure. However, as illustrated by Haltiner and Williams (1980, their section 1.8), wind vectors need a transformation between these two EL grids, including a mapping factor and the projection of wind components on the sphere onto the polar stereographic plane. In fact, this transformation has been incorporated in the Grid Analysis and Display System (GrADS) software routine (available online at http://grads.iges.org/grads/gadoc/). Although wind vectors (including magnitude and direction) cannot change from one grid to the other, their components along the ordinate and abscissa of the EA and OG grids differ from those along latitude and longitude of the EL grid. Thus, horizontal gradients of wind components in the former two grids are not the same as those on the latter grid. A procedure to project wind components, used in the analysis and depiction of the polar circulation, from the EL grid onto the EA and OG grids is needed and is presented below.

1) EA GRID

(i) Step 1: Projection of $\mathbf{V}_0$(EL) *onto the EA grid*

A wind vector cannot be changed in its magnitude and direction from one grid to the other. Because of this characteristic, the difference in orientations of the EL and EA grids is reflected by wind components displayed on these two grids (Fig. 2a). Wind components of a wind vector along longitude and latitude at the center of a concerned EA cell are designated as (u_0, v_0), and a gray square is formed by connecting centers of the EA cells surrounding a concerned EA cell (Fig. 2b). The distance from the center of this cell to an EL grid point within/on this square is d. The (u_0, v_0) components at this center are averages of (u, v) components of all wind vectors on the EL grid points within this square by a weighting factor of the inverse distance squared $(1/d^2)$. However, the (u_0, v_0) components are still projected along the orientation of the EL grid. Because the orientation of the EA grid (thin solid lines of Fig. 2b) is different from that of the EL grid (thin dashed lines of Fig. 2b), the newly formed (u_0, v_0) components are rotated to the orientation of the EA grid through the following relationship:

$$\begin{pmatrix} u' \\ v' \end{pmatrix} = \begin{pmatrix} \cos\theta & -\sin\theta \\ \sin\theta & \cos\theta \end{pmatrix} \begin{pmatrix} u_0 \\ v_0 \end{pmatrix}, \tag{3}$$

where θ is the longitude of the concerned EA cell center and (u', v') are components of the new wind vector $\mathbf{V}$(EA).

(ii) Step 2: Projection of $\mathbf{V}$(EA) *onto the EL grid*

A reversed transformation of $\mathbf{V}_0$(EL) onto the EA grid in step 1 is sometimes needed. The (u', v') components of wind vector $\mathbf{V}$(EA) at an EL grid point (Fig. 2c) within the gray box (same as that in Fig. 2b) can be obtained from the following approach: average wind components of $\mathbf{V}$(EA) on centers of the EA cells surrounding the center of an EA cell nearest the concerned EL grid with the weighting factor $1/d^2$, where d is the distance between this EL grid and the center of the designated EA cell within/on the gray square. The (u', v') wind components on an EL grid point are then rotated onto longitude and latitude with the following equations:

$$\begin{pmatrix} u_0 \\ v_0 \end{pmatrix} = \begin{pmatrix} \cos\theta & \sin\theta \\ -\sin\theta & \cos\theta \end{pmatrix} \begin{pmatrix} u' \\ v' \end{pmatrix}, \tag{4}$$

where θ is longitude of the EL grid point. This newly generated $\mathbf{V}_0$(EL) is averaged with the corresponding already existing $\mathbf{V}_0$(EL) and two other adjacent $\mathbf{V}_0$(EL) grid points to its north and south with a weighting factor of (1, 2, 1) over a 5° latitudinal merging zone centered at a given latitude determined by the need of the study.

2) OG GRID

Following the notation convention of Fig. 2, wind components of a wind vector $\mathbf{V}_0$ on the EL grid are designated as u_0 and v_0 along longitude and latitude, respectively, and those on the OG grid are designated as u' and v' along the ordinate and abscissa, respectively. The relationship between (u_0, v_0) and (u', v') is shown in Fig. 3a. The procedure to project $\mathbf{V}_0$(EL) onto the OG grid (Fig. 3b) or to project $\mathbf{V}$(OG) onto the EL grid (Fig. 3c) is the same as that used for the EA grid, except the inverse-distance-squared method used for the EA grid is replaced by the B-16 interpolation scheme. The 16 EL grid points (black dots in Fig. 3b) are those with their distances nearest to the concerned OG grid point (gray dot in Fig. 3b). In the same manner, the 16 OG grid points (gray dots in Fig. 3c) are those nearest to the concerned EL grid point.

b. (ψ, χ) and $(\mathbf{V}_R, \mathbf{V}_D)$

The data aggregation at high latitudes caused by the nonuniformity of data distribution results in the defor-

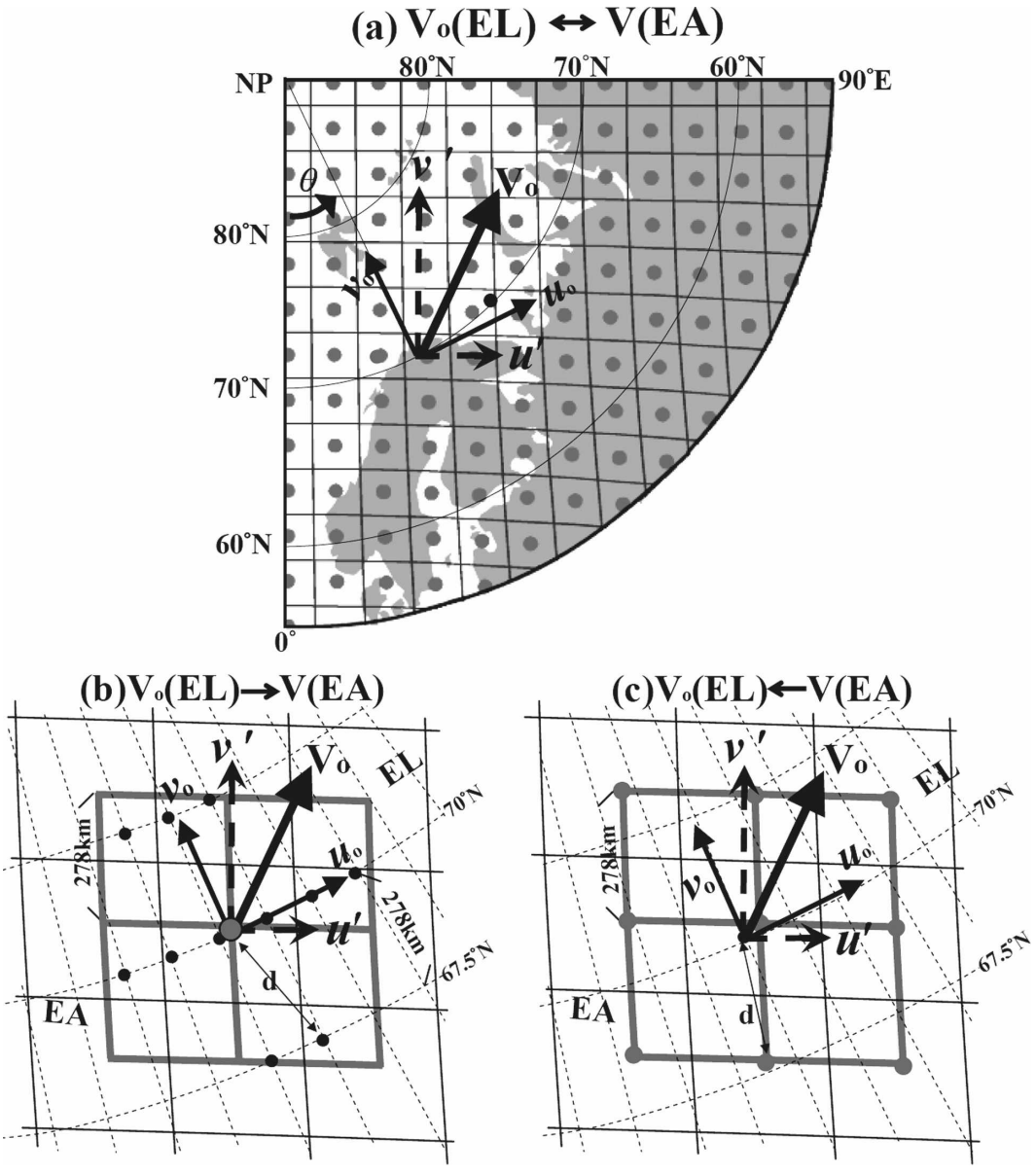

FIG. 2. (a) Transformation of wind components between EL and EA grids on the polar stereographic projection. Note that (u_0, v_0) are wind components along the longitudinal and latitudinal directions, respectively, on the EL grid and (u', v') are those along the row and column on the EA grid; θ is longitude. (b) The transformation of (u_0, v_0) components on the EL grid to the EA grid; (c) the reversed transformation.

mation of computed horizontal derivatives (e.g., vorticity and divergence) of wind fields and, in turn, the streamfunction and velocity potential derived from these horizontal derivatives. To circumvent this difficulty, an indirect computational strategy is adopted. Both ζ and D are computed first on the EA and OG grids. Because these two variables are scalars, their spatial structure may not be deformed by their interpolation from the EA and OG grids to the EL grid of the polar stereographic plane and then the projection onto the EL grid of the sphere. Then, both ψ and χ can be obtained by solving the Poisson equations with ζ and D as forcings, respectively, through an inverse spherical harmonics analysis. Similar to ζ and D, both ψ and χ (obtained on the EL grid of the sphere) are also scalars and can be interpolated onto the EA and OG grid without any deformation. The procedure adopted in this study to generate ψ and χ and rotation ($\mathbf{V}_R$) and divergent ($\mathbf{V}_D$) wind vectors on these grids is presented as follows:

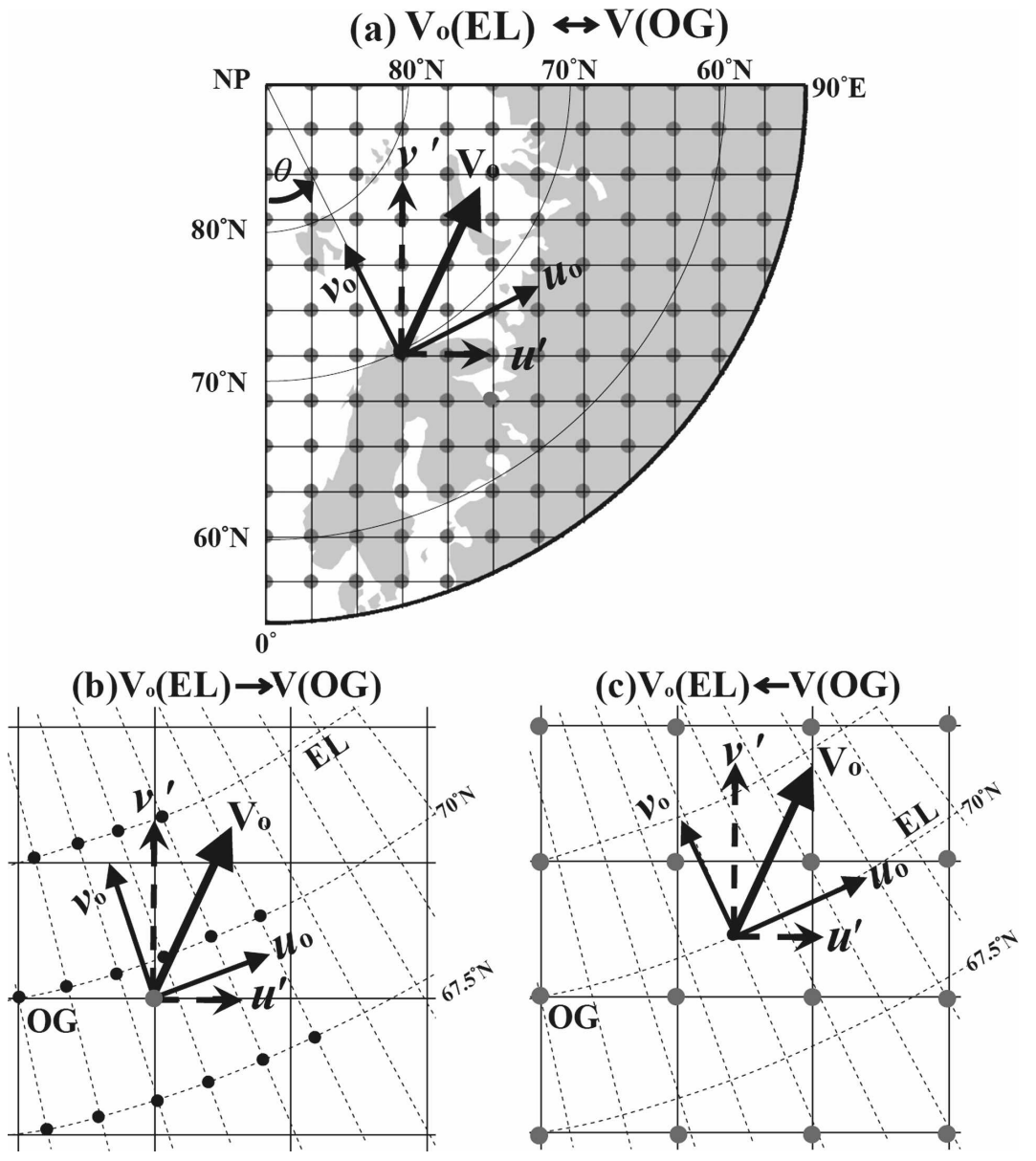

FIG. 3. As in Fig. 2, but for transformation of wind components between EL and OG grids: (u', v') are wind components along the ordinate and abscissa on the OG grid.

1) In step 1, using **V**(EA) generated in step 1 described in section 3a, vorticity and divergence are computed on the EA grid, (ζ', D')(EA). The vorticity and divergence on the polar side of a selected latitude φ are then interpolated to the EL grid by the inverse-distance-squared method and averaged with the original (ζ, D)(EL) over the merging zone of 5° latitude centered at latitude φ using a (1, 2, 1) weighting factor to form a new set of (ζ, D)(EL). The spatial relationship between the EA and EL grid can be inferred from Fig. 2.
2) In step 2, the newly created (ζ, D)(EL) of the polar stereographic plane is projected onto the EL grid of the sphere. Using the latter (ζ, D)(EL), the (ψ, χ) fields are generated by solving the Poisson equation through the NCAR global spectral toolkit (http://www.cisl.ucar.edu/css/software/spherepack/). The ($\mathbf{V}_R$, $\mathbf{V}_D$)(EL) fields of a sphere are then computed with (ψ, χ)(EL) through the following relationship: $\mathbf{V}_R = \hat{k} \times \nabla\psi$ and $V_D = \nabla\chi$.
3) In step 3, the (ψ, χ)(EL) fields are interpolated onto the EA grid with the inverse-distance-squared method to generate (ψ', χ')(EA). The ($\mathbf{V}'_R$, $\mathbf{V}'_D$)(EA) fields are then generated from (ψ',

χ')(EA). Following step 2 described in section 3a, ($\mathbf{V}'_R$, $\mathbf{V}'_D$)(EA) are merged with the ($\mathbf{V}_R$, $\mathbf{V}_D$)(EL) transformed from a sphere over a 5°-latitude merging zone centered at latitude ϕ. Eventually the (ψ', χ')(EA) and ($\mathbf{V}'_R$, $\mathbf{V}'_D$)(EL) on the polar stereographic plane are transformed to the EL grid of a sphere.

The procedures to generate (ψ', χ') and ($\mathbf{V}'_R$, $\mathbf{V}'_D$) on the OG grid and to merge these fields with those on the EL grid are exactly the same as those for the EA grid, except the inverse-distance-squared method is replaced by the B-16 interpolation scheme. To facilitate the comprehension of procedures presented in sections 3a and 3b, a flowchart summarizing these procedures is shown in Fig. 4 to supplement Figs. 2 and 3.

4. Comparison for analyses on different grids

Differences in spatial structure and procedure of data processing among the three grids were presented in section 3. The possible impacts of these differences on the depiction of the polar circulation are illustrated in terms of summer wind vectors, streamfunction, and velocity potential in the Arctic region. The goal of this effort is to search for the best grid to 1) resolve the aggregation of the EL wind vectors and 2) generate streamfunction and velocity potential using the EL wind vectors. Because the maximum Arctic westerlies in summer are located at 400 hPa (Yoon and Chen 2006), we shall concentrate the illustration of impacts on this level. The data used in this study were derived from ERA-40 archived on an EL grid of a sphere. These reanalyses were issued in two resolutions: 1.125° latitude × 1.125° longitude and 2.5° latitude × 2.5° longitude. To save storage space and to match other reanalyses, the latter version of ERA-40 for all summers during the 1979–2002 period was used in this study.

a. Wind vectors

The summer polar circulation at upper levels is characterized by three troughs (along the Bering Sea, eastern Baffin Island, and central Eurasia) and three ridges (along eastern Siberia, the Rocky Mountains, and eastern Europe; Yoon and Chen 2006). These salient features of the Arctic circulation emerge from the circumpolar vortex depicted by the 400-hPa geopotential height Z(400 hPa) superimposed with isotachs $|\mathbf{V}$(400 hPa)$|$ (Fig. 5a). Note that geopotential height is a first-order variable. Depictions of the salient features in the summer Arctic circulation using Z(400 hPa) are the same on the three grids (not shown) as those shown in Fig. 5a.

To portray the upper-level summer Arctic circulation, wind vectors are prepared on the three grids. For the RL grid (Fig. 5b), upper-air troughs and ridges of this summer circulation are not identifiable, except for the trough in eastern Baffin Island. In contrast, these salient features of this summer circulation are clearly recognized using $\mathbf{V}$(400 hPa) on the EA (Fig. 5c) and OG grids (Fig. 5d). The resemblance of salient circulation features depicted on these two grids implies that these grid systems may have the same merit. To verify this assessment, wind vectors on the EA grid are linearly interpolated (using the four-point bilinear interpolation) onto the OG grid. The difference between $\mathbf{V}$(400 hPa) on these two grids, $\Delta\mathbf{V}$(400 hPa), is shown in Fig. 5e using a streamline chart. A wavenumber-3 structure emerges from the $\Delta\mathbf{V}$(400 hPa) field. It is inferred from this wavenumber-3 structure that summer stationary waves projecting on the EA grid in the Arctic region are weaker (i.e., smaller in amplitude) than those on the OG grid. This difference is attributed to the difference in the analysis procedures used by these two grids to generate wind vectors. For the EA grid, wind vectors at the center of a cell are calculated using the average of all available EL wind vectors within cells surrounding a concerned EA cell with a weighting factor of $1/d^2$ from this cell center. The B-16 interpolation is used in preparing wind vectors on the OG grid with the surrounding EL wind vectors. The difference in depicting the Arctic circulation between the EA and OG grids suggests that the presentation of Arctic interannual variation modes, such as the Arctic Oscillation (Thompson and Wallace 2000; Thompson et al. 2000), should be carefully calibrated depending on the grid used.

b. Streamfunction and velocity potential

The Northern Hemisphere circulation in summer is dominated by the Asian, North American, and West African monsoons. Separated by the North Pacific Ocean and North Atlantic Ocean troughs, the former two monsoons are characterized by the Tibetan and Mexican highs, respectively, in the upper troposphere. These salient features of the summer tropical circulation are depicted well by the streamfunction (Krishnamurti 1971). To examine the maintenance mechanism of these circulation features, Krishnamurti (1971) introduced velocity potential χ. These monsoons are maintained by the east–west differential heating through the Sverdrup relation reflected by a spatial quadrature χ–ψ relationship and a vertical phase reversal of ψ (Chen 2003). White (1982) showed that stationary waves at high latitudes exhibit a vertically uniform structure, but the dynamics of these waves have not been explored. The χ–ψ of Arctic stationary waves exhibits a spatial quadrature relationship, and the vorticity budget analy-

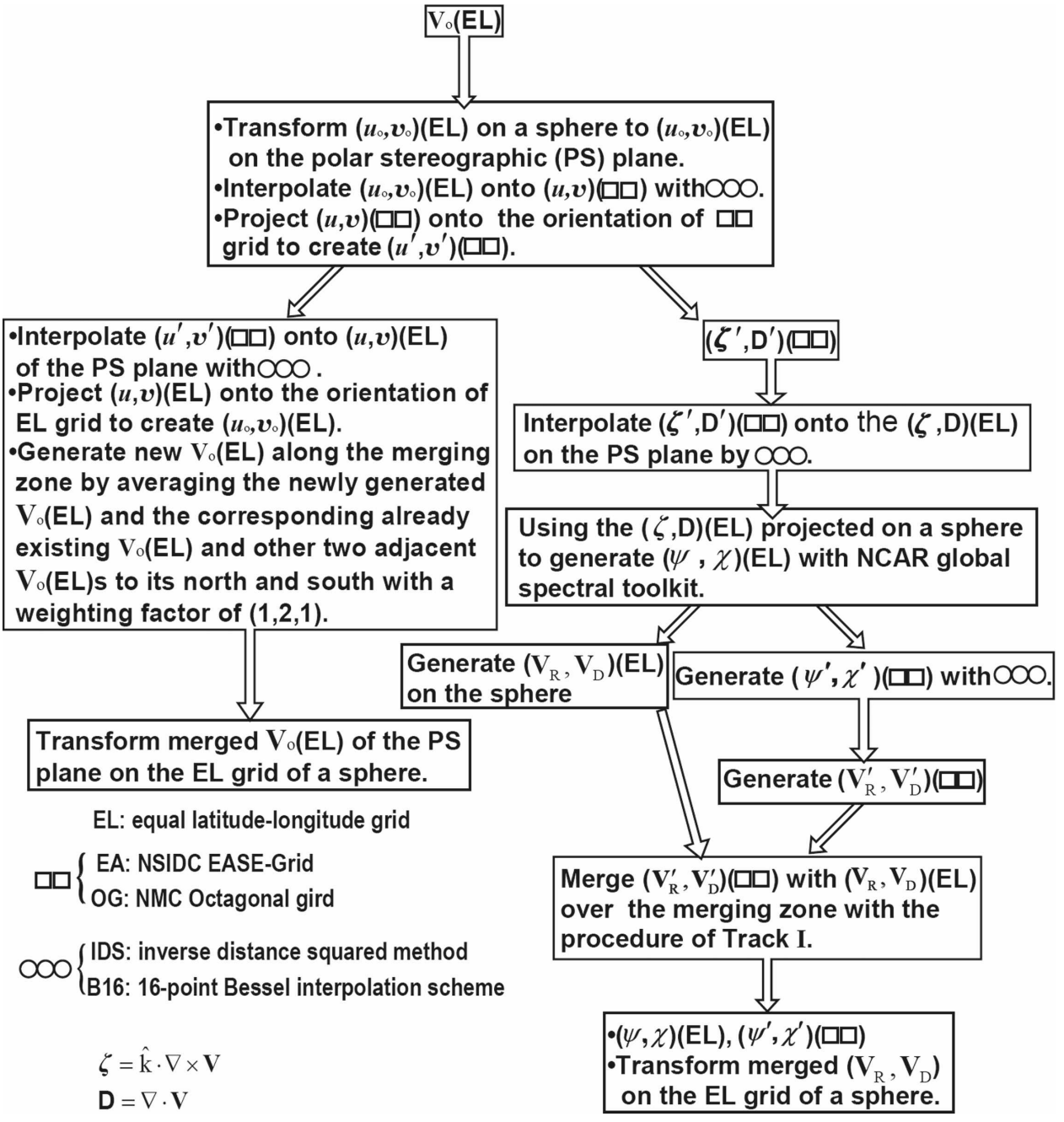

FIG. 4. A flowchart to illustrate the proposed procedure of projecting meteorological data analyzed in the EL grid onto the EA or OG grid: 1) project wind vectors $\mathbf{V}_0$ of the EL grid on the EA or OG grid (track I on the left) and 2) generate streamfunction ψ and velocity potential χ on both the EL and EA (or OG) grids by solving the Poisson equation using forcings (ζ, D)(EL) south of latitude φ and the projection of (ζ', D')(EA) [or (ζ', D')(OG)] on the EL grid north of latitude φ (track II on the right); ($\mathbf{V}'_R$, $\mathbf{V}'_D$)(EA) [or ($\mathbf{V}'_R$, $\mathbf{V}'_D$)(OG)] north of latitude φ and ($\mathbf{V}_R$, V_D)(EL) south of latitude φ merge at this latitude.

sis reveals that the basic dynamics of these "equivalent barotropic waves" at high latitudes belong to an Arctic regime in which the vortex stretching is primarily balanced by the relative vorticity advection (T.-C. Chen 2008, unpublished manuscript). It is evident that the spatial structure and spatial relationship of the ψ and χ fields, and the basic dynamics of the polar circulation, are useful in assessing the quality of these two variables generated on different grids.

The ψ and χ fields are generally obtained by solving

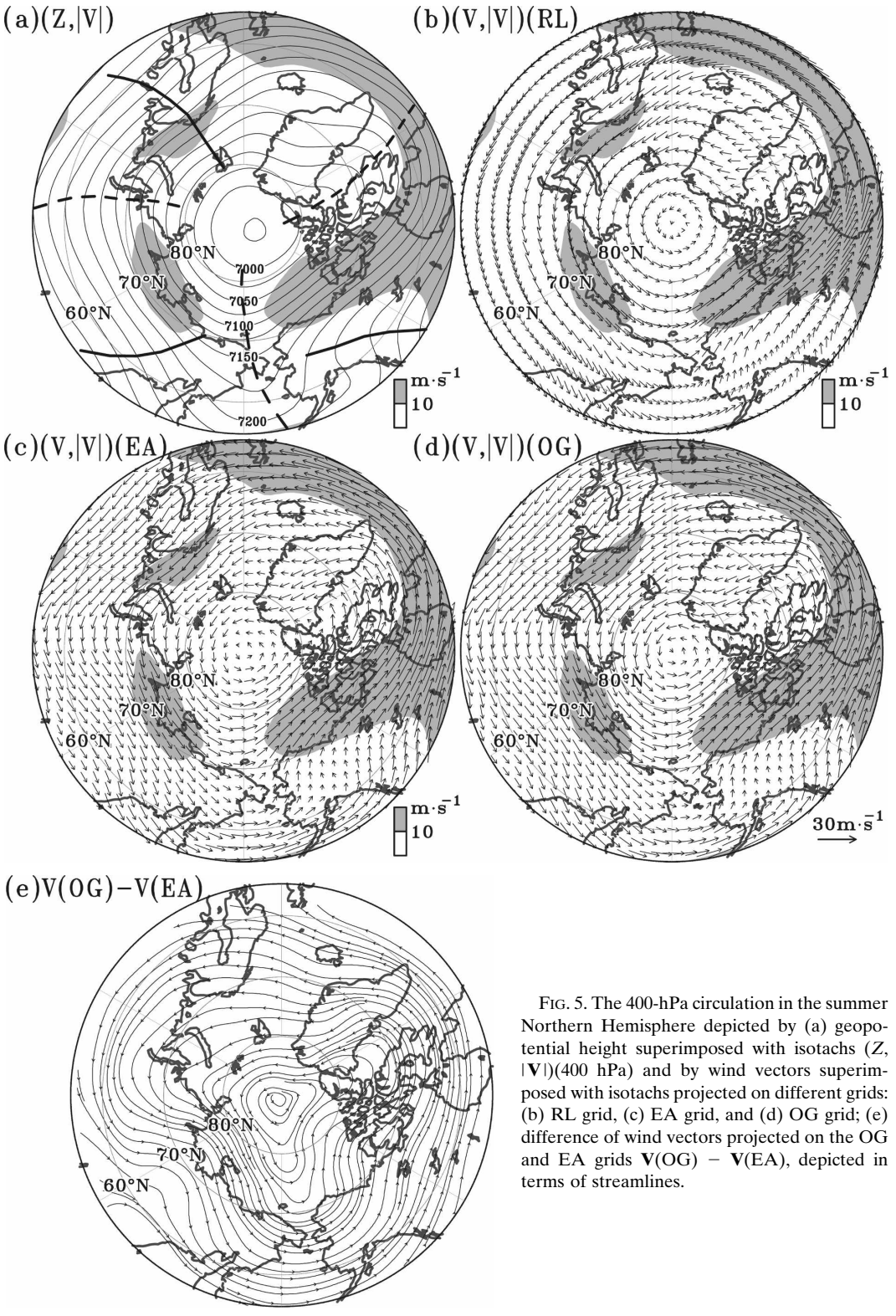

FIG. 5. The 400-hPa circulation in the summer Northern Hemisphere depicted by (a) geopotential height superimposed with isotachs (Z, $|\mathbf{V}|$)(400 hPa) and by wind vectors superimposed with isotachs projected on different grids: (b) RL grid, (c) EA grid, and (d) OG grid; (e) difference of wind vectors projected on the OG and EA grids $\mathbf{V}$(OG) − $\mathbf{V}$(EA), depicted in terms of streamlines.

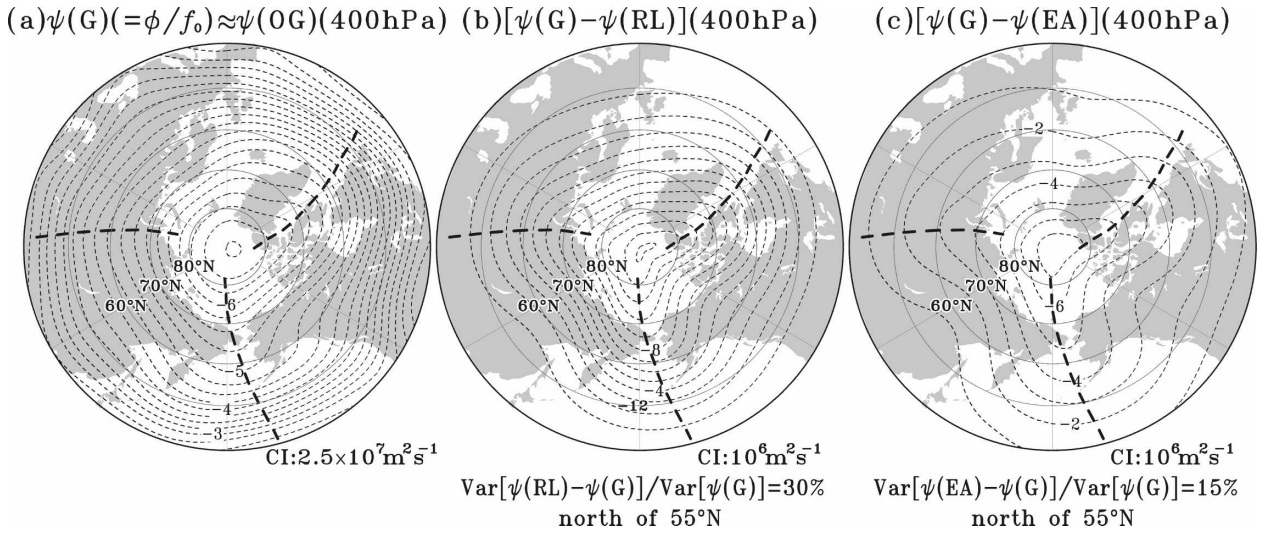

FIG. 6. The (a) ψ(G)(400 hPa) generated using geopotential ϕ(400 hPa) [= gZ(400 hPa), where Z(400 hPa) is shown in Fig. 5a]; (b) [ψ(G) − ψ(RL)](400 hPa), where ψ(RL) is obtained using ζ(400 hPa) computed on the RL grid; and (c) [ψ(G) − ψ(EA)](400 hPa), where ψ(EA)(400 hPa) is generated using ζ(400 hPa) computed on the EA grid. The contour interval of ψ(G)(400 hPa) is 2.5×10^7 m^2 s^{-1}, and that of [ψ(G) − ψ(RL)](400 hPa) and [ψ(G) − ψ(EA)](400 hPa) is 10^6 m^2 s^{-1}. Variance ratios of Var[ψ(RL) − ψ(G)]/Var[ψ(G)] and Var[ψ(EA) − ψ(G)]/Var[ψ(G)] averaged north of 55°N are also added to the bottoms of (b) and (c), respectively.

the Poisson equation with ζ and D as forcings [Eqs. (1) and (2)], with computations of ζ and D requiring derivatives of horizontal winds. Using winds archived on the EL grid, the data aggregation toward the Poles and the spatial nonuniformity distort calculations of ζ and D relative to those computed with a uniform spatial distribution at high latitudes. As a consequence, the ψ and χ fields obtained using the improperly computed ζ and D, respectively, may contain significant errors at high latitudes. Accurate depictions of the Arctic circulation using the ψ and χ fields require proper solutions for these two variables. Because the maximum Arctic westerlies in summer are located at 400 hPa, the summer ψ and χ fields at this level are used to illustrate the difference among the depictions of the Arctic summer circulation on the three grids.

Following the procedure given in section 3, the ψ and χ fields generated from the ζ and D fields are displayed in Figs. 6 and 7, respectively. At high latitudes, the Coriolis parameter $f_0 = 2\Omega \sin\varphi$ does not change significantly. Based on the geostrophy $\psi = \phi/f_0$, the streamfunction can be derived from the geopotential ϕ. Using Z(400 hPa) shown in Fig. 5a, the 400-hPa streamfunction, ψ(G)(400 hPa), is displayed in Fig. 6a. Three major troughs (thick dashed lines) are apparent using ψ(G)(400 hPa). The 400-hPa streamfunction generated directly from ζ(400 hPa) projected on the OG grid north (south) of 45°N (°S), ψ(OG)(400 hPa) (not shown), can be verified against ψ(G)(400 hPa) using a variance (Var) ratio: Var[ψ(OG) − ψ(G)]/Var[ψ(G)]. North of 55°N, this ratio is approximately 0.5%. Thus, the difference between ψ(G)(400 hPa) and ψ(OG)(400 hPa) is negligible. This allows the former to be used as a proxy of the latter to verify streamfunction obtained on the RL and EA grids: north of 55°N, Var[ψ(RL) − ψ(G)]/Var[ψ(G)] = 30% and Var[ψ(EA) − ψ(G)]/Var[ψ(G)] = 15%. It is inferred from these variance ratios that noticeable differences exist between ψ(G) and ψ(RL) and more moderate differences exist between ψ(G) and ψ(EA). To understand the spatial structure of these differences, ψ(G) − ψ(RL) and ψ(G) − ψ(EA) are shown in Figs. 6b and 6c, respectively. Summer stationary waves in the Arctic depicted on the EA grid are weaker (as revealed from Fig. 6c), and those on the RL grid are much weaker (as indicated by the contrast between Figs. 6b and 6c).

The variance of χ(200 hPa) in summer contributed by wavenumbers-1–2 is over 90% in the tropics (Krishnamurti 1971; Chen 2003). As shown in Fig. 7a, the χ(RL)(400 hPa) field is primarily formed by the ultralong-wave regime at low and high latitudes. Air mass diverges out of the Asian monsoon hemisphere and converges toward the other hemisphere. It is inferred from the nearly featureless ψ(RL)(400 hPa) and χ(RL)(400 hPa) fields in the Arctic that ζ(400 hPa) and D(400 hPa) are oversmoothed on the RL grid. Along the latitude circle at 60°N, a wavenumber-3 structure of the divergent circulation is expected to couple with the three troughs and ridges of the ψ(G)(400 hPa) spatial structure (Fig. 6a). To illustrate better the χ–ψ relation-

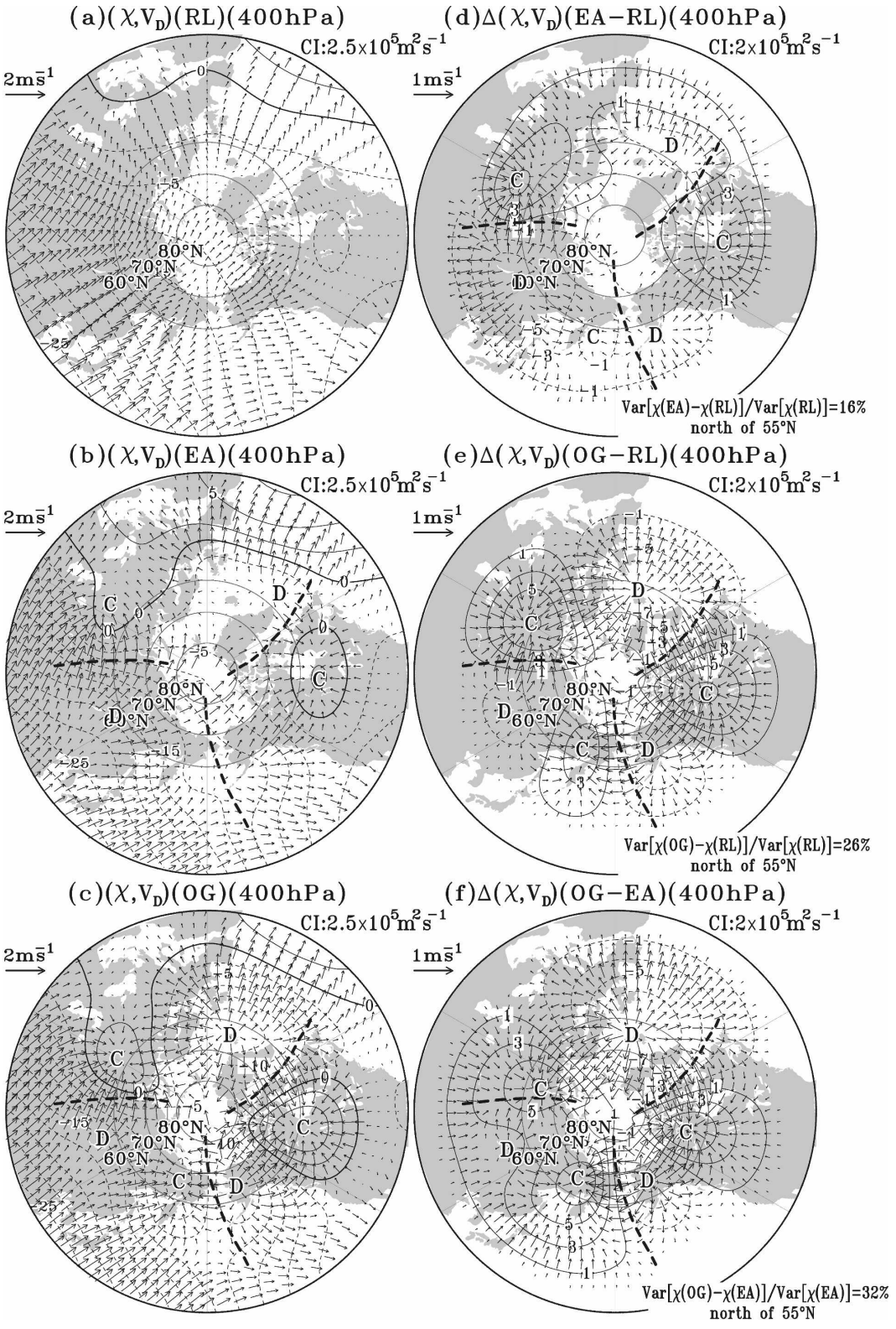

FIG. 7. Velocity potential χ(400 hPa) and divergent wind vector $\mathbf{V}_D$(400 hPa) generated on the (a) RL grid, (b) EA grid, (c) OG grid, and the difference of (χ, $\mathbf{V}_D$)(400 hPa) between (d) EA and RL grids, (e) OG and RL grids, and (f) OG and EA grids. Contour intervals of χ(400 hPa) and $\Delta\chi$(400 hPa) are 2.5×10^5 m^2 s^{-1} and 2×10^5 m^2 s^{-1}, respectively. Variance ratios of Var[χ(EA) − χ(RL)]/Var[χ(RL)], Var[χ(OG) − χ(RL)]/Var[χ(RL)], Var[χ(OG) − χ(EA)]/Var[χ(EA)] averaged north of 55°N are added in the bottoms of (e) and (f).

ship of Arctic stationary waves, the convergent and divergent centers of χ(400 hPa) indicated by the superimposed $\mathbf{V}_D$(400 hPa) are marked by C and D, respectively. The wavenumber-3 structure is not particularly discernable using (χ, $\mathbf{V}_D$)(EA)(400 hPa) (Fig. 7b) but becomes clear in [(χ, $\mathbf{V}_D$)(EA) − (χ, V_D)(RL)](400 hPa) (Fig. 7d). In contrast, the wavenumber-3 relationship stands out clearly from the divergent circulation depicted on the OG grid (χ, $\mathbf{V}_D$)(OG)(400 hPa) (Fig. 7c) and is more discernable from [(χ, $\mathbf{V}_D$)(OG) − (χ, $\mathbf{V}_D$)(RL)](400 hPa) (Fig. 7e). Although no observed χ field is available to validate χ(OG)(400 hPa), the relationship between the divergent circulation and the upper-level short wave (T.-C. Chen 2008, unpublished manuscript) offers us a qualitative means to pursue this validation. Troughs of midlatitude stationary waves are spatially in quadrature with the east–west circulation with divergent centers ahead of them and convergent centers behind them, and the opposite relationship appears between ridges and divergent/convergent centers (Lau 1979; Chen 2005). The contrast between ψ(OG)(400 hPa) and χ(OG)(400 hPa) shows that their relationship matches T.-C. Chen's (2008, unpublished manuscript) observation. It is apparent that the OG grid produces more-realistic ψ(400 hPa) and χ(400 hPa) fields, which is further confirmed by the clear wavenumber-3 structure in the difference of divergent circulation between the OG and EA grids (Fig. 7f).

The summer Arctic circulation characterized by three upper-level troughs is depicted well by ψ(OG)(400 hPa). As expected from the Arctic stationary wave regime, the divergent circulation coupled with these Arctic troughs is correctly depicted by (χ, $\mathbf{V}_D$)(OG)(400 hPa). It is clear that the procedure outlined in Track II in Fig. 4 can properly generate derived variables to portray the Arctic circulation in a hemispheric perspective. Depiction of the Arctic circulation and the validation of simulations by global climate models require a delicate graphical procedure.

5. Concluding remarks

The possible impact of polar circulation change on the global climate has recently attracted more research attention. Because the polar circulation is part of the global circulation, this impact must be clearly illustrated in a hemispheric/global perspective. Globally assimilated observational and forecast data are usually archived on a rectangular latitude–longitude grid. For this reason, the polar circulation is often depicted by this grid on the polar stereographic projection. Because of the decrease in the circumference around latitude circles toward the Poles, the east–west spatial interval between two grid points on the equal latitude–longitude grid is reduced. The data aggregation caused by this spatial nonuniformity may result in a deformation of the polar circulation depicted by the wind vectors and derived variables. From a practical point of view, it is not possible to portray the polar circulation using modern reanalyses without a proper grid. To present meteorological field variables in the polar regions, three grids have been adopted in meteorological research: the reduced latitude–longitude grid, the NSIDC EASE grid, and the NMC octagonal grid. A systematic comparison of the summer Arctic circulation depicted using wind vectors $\mathbf{V}$, streamfunction ψ, and velocity potential χ on these three grids was made to identify the merits and disadvantages of these grid systems when computing derivatives to obtain one set of circulation diagnostics from another. Our five major findings are as follows:

1) Scalar variables exhibit the same structure on all three grids.
2) Globally assimilated observational data are usually archived on the rectangular latitude–longitude (2.5° latitude × 2.5° longitude) grid and are often displayed on the RL grid. Orientations of the EA and OG grids differ from the RL grid. Wind components projected on latitude and longitude points need to be reprojected on the rows and columns of the EA grid and on the ordinate and abscissa of the OG grid to calculate gradients of wind components (e.g., vorticity and divergence) in the two latter grids.
3) The most commonly adopted approach to display globally archived data is the RL grid, but the summer Arctic troughs and ridges are not well recognizable with wind vectors displayed on this grid. These circulation features have to be depicted with the EA and OG grids. The amplitudes of these troughs and ridges (i.e., summer Arctic stationary waves) are stronger on the OG grid than on the EA grid.
4) Relative to the streamfunction ψ(G) obtained using geopotential height through geostrophy, the streamfunction ψ(OG) obtained with vorticity computed on the OG grid has only about 0.5% error. Errors in the streamfunction obtained with vorticity computed on the RL and EA grids are 30% and 15%, respectively.
5) Perturbations of ψ in the Arctic region exhibit a vertically uniform structure (White 1982), but χ and ψ of Arctic troughs have a spatial quadrature relationship: the divergent (convergent) center is located ahead (behind) the Arctic trough. The (χ, $\mathbf{V}_D$)(OG) field shows a better fit with the ψ(G) field than do the (χ, $\mathbf{V}_D$)(RL) and (χ, $\mathbf{V}_D$)(EA) fields.

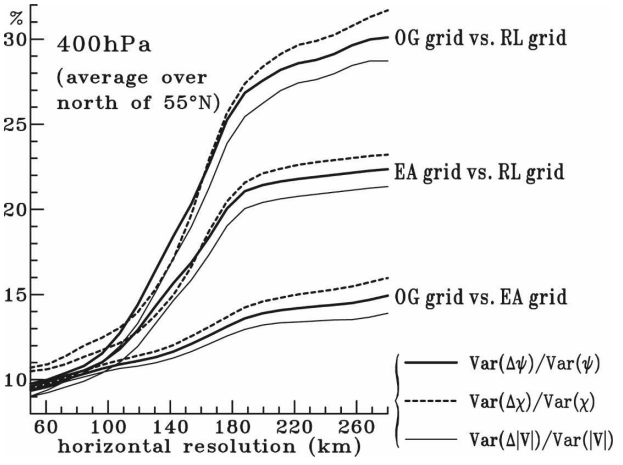

FIG. 8. Impact of resolution presented by variance (Var) ratios (or errors) of three meteorological variables ($|\mathbf{V}|$, ψ, and χ at 400 hPa) generated on different grids. These grids are indicated on each group of variance ratios, where $\Delta(\,) = (\,)$(yy grid) $-$ $(\,)$(xx grid) and var( ) = variance of ( ) on the yy grid. For example, yy and xx grids in the top group represent OG and RL grids, respectively.

The EA grid has been widely used in high-resolution regional Arctic climate modeling (e.g., Jürrens 1999), and the RL grid is often used to present results from global climate models (e.g., DeWeaver and Bitz 2006; Hack et al. 2006; Turner et al. 2006). Of the three grids used to depict the Arctic summer circulation, the OG grid seems to be the most representative. However, this assessment is made with caution for the following two reasons:

1) The findings are based on ERA-40 with a resolution of 2.5° latitude × 2.5° longitude (~278 km × 278 km). Errors of **V**, ψ, and χ on one grid against the other with different resolutions are shown in Fig. 8. It is clearly indicated that all three variables on the three grids may have a difference of approximately 10% when the resolution is close to 50 km.
2) The meteorological field variables on the OG grid need to be merged with those on the EL grid to gain a hemisphere perspective. Nevertheless, to maintain the singularity of the polar circulation with the OG grid, the merger between the OG and EL grid at any given latitude is perhaps the best strategy in depicting the polar circulation in the context of a hemispheric perspective.

Acknowledgments. This study was supported partially by the NASA NSIPP Grant NAG-58293. Author Gutowski's contribution to this study was supported by the NSF Grant OPP-0229559 and DOE Grant DE-FG02-07ER64463. The technique support and editorial comments provided by Simon Wang and Adam Clark, respectively, are greatly appreciated. Comments and suggestions offered by reviewers of this paper were very helpful in improving it. Following the suggestion of one reviewer, the FORTRAN subroutine of the data processing schemes for the three grids presented in this paper is posted on the institutional Web site (http://tmchen.iastate.edu/Polar_grids/).

REFERENCES

Armstrong, R. L., and M. J. Brodzik, 1995: An earth-grid SSM/I data set for cryospheric studies and global change monitoring. *Adv. Space Res.,* **16,** 115–163.

Bedient, H. A., W. G. Collins, and G. Dent, 1967: An operational tropical analysis system. *Mon. Wea. Rev.,* **95,** 942–949.

Bormann, N., and J.-N. Thépaut, 2004: Impact of MODIS polar winds in ECMWF's 4DVAR data assimilation system. *Mon. Wea. Rev.,* **132,** 929–940.

Brodzik, M. J., and K. W. Knowles, 2002: EASE-Grid: A versatile set of equal-area projections and grids. *Discrete Global Grids,* M. Goodchild, Ed., National Center for Geographic Information and Analysis. [Available online at http://www.ncgia.ucsb.edu/globalgrids-book/ease_grid/.]

Burrows, W. R., 1974: Merging of data on NMC, octagonal and Mercator grids for hemispheric analysis. *Mon. Wea. Rev.,* **102,** 76–81.

Chen, T.-C., 2003: Maintenance of summer monsoon circulations: A planetary-scale perspective. *J. Climate,* **16,** 2022–2037.

——, 2005: The structure and maintenance of stationary waves in the winter Northern Hemisphere. *J. Atmos. Sci.,* **62,** 3637–3660.

DeWeaver, E., and C. M. Bitz, 2006: Atmospheric circulation and its effect on Arctic sea ice in CCSM3 simulations at medium and high resolution. *J. Climate,* **19,** 2415–2436.

Galantowicz, J. F., and A. W. England, 1991: The Michigan Earth Grid: Description, registration method for SSM/I data, and derivative map projections. Radiation Laboratory, Department of Electrical Engineering and Computer Science Tech. Rep. 027396-2-T, University of Michigan, 19 pp.

Hack, J. J., J. M. Caron, G. Danabasoglu, K. W. Olson, C. M. Bitz, and J. E. Truesdale, 2006: CCSM–CAM3 climate simulation sensitivity to changes in horizontal resolution. *J. Climate,* **19,** 2267–2289.

Haltiner, G. J., and R. T. Williams, 1980: *Numerical Prediction and Dynamical Meteorology*. 2nd ed. John Wiley and Sons, 470 pp.

Jenne, R., 1975: Format for Northern Hemisphere octagonal grid data. NCAR Tech. Doc., 8 pp. [Available online at http://dss.ucar.edu/datasets/common/nmc.octagon/format.]

Jürrens, R., 1999: Validation of surface fluxes in climate simulations of the Arctic with the regional model REMO. *Tellus,* **51A,** 698–709.

Kanamitsu, M., W. Ebisuzaki, J. Woollen, S.-K. Yang, J. J. Hnilo, M. Fiorino, and G. L. Potter, 2002: NCEP–DOE AMIP-II Reanalysis (R-2). *Bull. Amer. Meteor. Soc.,* **83,** 1631–1643.

Krishnamurti, T. N., 1971: Tropical east-west circulations during the northern summer. *J. Atmos. Sci.,* **28,** 1342–1347.

——, M. Kanamitsu, W. J. Koss, and J. D. Lee, 1973: Tropical east–west circulations during the northern winter. *J. Atmos. Sci.,* **30,** 780–787.

Kurihara, Y., 1965: Numerical integration of the primitive equations on a spherical grid. *Mon. Wea. Rev.,* **93,** 399–415.

Lau, N. C., 1979: The structure and energetics of transient disturbances in the Northern Hemisphere wintertime circulation. *J. Atmos. Sci.,* **36,** 982–995.

Onogi, K., and Coauthors, 2005: JRA-25: Japanese 25-year reanalysis project—Progress and status. *Quart. J. Roy. Meteor. Soc.,* **131,** 3259–3268.

Parry, M., O. Canziani, J. Palutikof, P. van der Linden, and C. Hanson, Eds., 2007: *Climate Change 2007: Impacts, Adaptation and Vulnerability.* Cambridge University Press, 976 pp.

Peixoto, J. P., and A. H. Oort, 1992: *Physics of Climate.* American Institute of Physics, 520 pp.

Shuman, F. G., and J. B. Hovermale, 1968: An operational six-layer primitive equation model. *J. Appl. Meteor.,* **7,** 525–547.

Simmonds, I., 1978: The application of a multi-level spectral model to data assimilation. *J. Atmos. Sci.,* **35,** 1321–1339.

Thompson, D. W. J., and J. M. Wallace, 2000: Annular modes in the extratropical circulation. Part I: Month-to-month variability. *J. Climate,* **13,** 1000–1016.

——, ——, and G. C. Hegerl, 2000: Annular modes in the extratropical circulation. Part II: Trends. *J. Climate,* **13,** 1018–1036.

Turner, J., W. M. Connolley, T. A. Lachlan-Cope, and G. J. Marshall, 2006: The performance of the Hadley Centre Climate Model (HadCM3) in high southern latitudes. *Int. J. Climatol.,* **26,** 91–112.

Uppala, S. M., and Coauthors, 2005: The ERA-40 re-analysis. *Quart. J. Roy. Meteor. Soc.,* **131,** 2961–3012.

White, G. H., 1982: An observational study of the Northern Hemisphere extratropical summertime general circulation. *J. Atmos. Sci.,* **39,** 24–40.

Yoon, J.-H., and T.-C. Chen, 2006: Maintenance of the boreal forest rainbelts during northern summer. *J. Climate,* **19,** 1437–1449.